Performance of NbSi transition-edge sensors readout with a 128 MUX factor for the QUBIC experiment

M. Salatino, B. Bélier, C. Chapron, D.T. Hoang, S. Maestre, S. Marnieros, W. Marty, L. Montier, M. Piat, D. Prêle, et al.

PROCEEDINGS OF SPIE

SPIEDigitalLibrary.org/conference-proceedings-of-spie

Performance of NbSi transition-edge sensors readout with a 128 MUX factor for the QUBIC experiment

M. Salatino, B. Bélier, C. Chapron, D. T. Hoang, S. Maestre, et al.

M. Salatino, B. Bélier, C. Chapron, D. T. Hoang, S. Maestre, S. Marnieros, W. Marty, L. Montier, M. Piat, D. Prêle, D. Rambaud, J. P. Thermeau, S. A. Torchinsky, S. Henrot-Versillé, F. Voisin, P. Ade, G. Amico, D. Auguste, J. Aumont, S. Banfi, G. Barbarán, P. Battaglia, E. Battistelli, A. Baù, D. Bennett, L. Bergé, J.-Ph. Bernard, M. Bersanelli, M.-A. Bigot-Sazy, N. Bleurvacq, J. Bonaparte, J. Bonis, G. Bordier, E. Bréelle, E. Bunn, D. Burke, D. Buzi, A. Buzzelli, F. Cavaliere, P. Chanial, R. Charlassier, F. Columbro, G. Coppi, A. Coppolecchia, F. Couchot, R. D'Agostino, G. D'Alessandro, P. de Bernardis, G. De Gasperis, M. De Leo, M. De Petris, A. Di Donato, L. Dumoulin, A. Etchegoyen, A. Fasciszewski, C. Franceschet, M. M. Gamboa Lerena, B. García, X. Garrido, M. Gaspard, A. Gault, D. Gayer, M. Gervasi, M. Giard, Y. Giraud-Héraud, M. Gómez Berisso, M. González, M. Gradziel, L. Grandsire, E. Guerrard, J.-Ch. Hamilton, D. Harari, V. Haynes, F. Incardona, E. Jules, J. Kaplan, A. Korotkov, C. Kristukat, L. Lamagna, S. Loucatos, T. Louis, A. Lowitz, V. Lukovic, R. Luterstein, B. Maffei, S. Masi, A. Mattei, A. J. May, M. A. McCulloch, M. C. Medina, L. Mele, S. Melhuish, A. Mennella, L. M. Mundo, J. A. Murphy, J. D. Murphy, C. O'Sullivan, E. Olivieri, A. Paiella, F. Pajot, A. Passerini, H. Pastoriza, A. Pelosi, C. Perbost, O. Perdereau, F. Pezzotta, F. Piacentini, L. Piccirillo, G. Pisano, G. Polenta, R. Puddu, P. Ringegni, G. E. Romero, A. Schillaci, C. G. Scóccola, S. Scully, S. Spinelli, M. Stolpovskiy, F. Suarez, A. Tartari, P. Timbie, M. Tristram, V. Truongcanh, C. Tucker, G. Tucker, S. Vanneste, D. Viganò, N. Vittorio, B. Watson, F. Wicek, M. Zannoni, A. Zullo, "Performance of NbSi transition-edge sensors readout with a 128 MUX factor for the QUBIC experiment," Proc. SPIE 10708, Millimeter, Submillimeter, and Far-Infrared Detectors and Instrumentation for Astronomy IX, 1070845 (9 July 2018); doi: 10.1117/12.2312080

SPIE.

Event: SPIE Astronomical Telescopes + Instrumentation, 2018, Austin, Texas, United States

Performance of NbSi Transition-Edge Sensors readout with a 128 MUX factor for the QUBIC experiment

M. Salatino[a], B. Bélier[b], C. Chapron[a], D.T. Hoang[a,ff], S. Maestre[c], S. Marnieros[d], W. Marty[c], L. Montier[c], M. Piat[a], D. Prêle[a], D. Rambaud[c], G. Stankowiak[a], J. P. Thermeau[a], S.A. Torchinsky[a], S. Henrot-Versillé[e], F. Voisin[a], P. Ade[f], G. Amico[g,h], D. Auguste[e], J. Aumont[i], S. Banfi[l,m], G. Barbarán[n], P. Battaglia[o], E. Battistelli[g,h], A. Baù[l,m], D. Bennett[p], L. Bergé[d], J.-Ph. Bernard[c], M. Bersanelli[o], M.-A. Bigot-Sazy[a], N. Bleurvacq[a], J. Bonaparte[q], J. Bonis[e], G. Bordier[a], E. Bréelle[a], E. Bunn[r], D. Burke[p], D. Buzi[g,h], A. Buzzelli[s,t], F. Cavaliere[o], P. Chanial[a], R. Charlassier[a], F. Columbro[g,h], G. Coppi[u], A. Coppolecchia[g,h], F. Couchot[e], R. D'Agostino[s], G. D'Alessandro[g,h], P. de Bernardis[g,h], G. De Gasperis[s,t], M. De Leo[g,h], M. De Petris[g,h], A. Di Donato[q], L. Dumoulin[d], A. Etchegoyen[v], A. Fasciszewski[q], C. Franceschet[o], M.M. Gamboa Lerena[w], B. García[v], X. Garrido[e], M. Gaspard[e], A. Gault[x], D. Gayer[p], M. Gervasi[l,m], M. Giard[c], Y. Giraud-Héraud[a], M. Gómez Berisso[y], M. González[y], M. Gradziel[p], L. Grandsire[a], E. Guerrard[e], J.-Ch. Hamilton[a], D. Harari[y], V. Haynes[u], F. Incardona[o], E. Jules[e], J. Kaplan[a], A. Korotkov[z], C. Kristukat[aa], L. Lamagna[g,h], S. Loucatos[a], T. Louis[e], A. Lowitz[x], V. Lukovic[s], R. Luterstein[n], B. Maffei[i], S. Masi[g,h], A. Mattei[h], A.J. May[u], M.A. McCulloch[u], M.C. Medina[bb], L. Mele[g,h], S. Melhuish[u], A. Mennella[o], L.M. Mundo[cc], J.A. Murphy[p], J.D. Murphy[p], C. O'Sullivan[p], E. Olivieri[d], A. Paiella[g,h], F. Pajot[c], A. Passerini[l,m], H. Pastoriza[y], A. Pelosi[h], C. Perbost[a], O. Perdereau[e], F. Pezzotta[o], F. Piacentini[g,h], L. Piccirillo[u], G. Pisano[f], G. Polenta[g,h], R. Puddu[g,h], P. Ringegni[cc], G.E. Romero[bb], A. Schillaci[g,dd], C.G. Scóccola[w], S. Scully[ee], S. Spinelli[l], M. Stolpovskiy[a], F. Suarez[v], A. Tartari[a], P. Timbie[x], M. Tristram[e], V. Truongcanh[e], C. Tucker[f], G. Tucker[z], S. Vanneste[e], D. Viganò[o], N. Vittorio[s,t], B. Watson[u], F. Wicek[e], M. Zannoni[l,m], and A. Zullo[h]

[a]Laboratoire AstroParticule et Cosmologie (APC), CNRS-IN2P3, Paris, France
[b]Centre de Nanosciences et de Nanotechnologies, Orsay, France
[c]Institut de Recherche en Astrophysique et Planétologie (CNRS-INSU), Toulouse, France
[d]Centre de Sciences Nucléaires et de Sciences de la Matière (CNRS-IN2P3), Orsay, France
[e]Laboratoire de l'Accélérateur Linéaire (CNRS-IN2P3), Orsay, France
[f]Cardiff University, Cardiff, UK
[g]Università di Roma - La Sapienza, Rome, Italy
[h]INFN, Sezione di Roma 1, Rome, Italy
[i]Institut d'Astrophysique Spatiale (CNRS-INSU), Orsay, France
[l]Università di Milano-Bicocca, Milan, Italy
[m]INFN Milano-Bicocca, Milan, Italy
[n]Regional Noroeste (CNEA), Salta, Argentina
[o]Università degli studi di Milano, Milan, Italy
[p]National University of Ireland, Maynooth, Ireland
[q]Centro Atómico Constituyentes (CNEA), Buenos Aires, Argentina
[r]University of Richmond, Richmond, VA, USA
[s]Università di Roma - Tor Vergata, Rome, Italy
[t]INFN, Sezione di Roma 2, Rome, Italy
[u]Jodrell Bank Centre for Astrophysics, University of Manchester, Manchester, UK

Millimeter, Submillimeter, and Far-Infrared Detectors and Instrumentation for Astronomy IX,
edited by Jonas Zmuidzinas, Jian-Rong Gao, Proc. of SPIE Vol. 10708, 1070845
 · doi: 10.1117/12.2312080

[v]Instituto de Tecnologías en Detección y Astropartículas (CNEA, CONICET, UNSAM), Godoy Cruz, Argentina
[w]Facultad de Cs Astronómicas y Geofísicas (Universidad Nacional de La Plata), CONICET, La Plata, Argentina
[x]University of Wisconsin, Madison, WI, USA
[y]Centro Atómico Bariloche and Instituto Balseiro (CNEA), Bariloche, Argentina
[z]Brown University, Providence, RI, USA
[aa]Escuela de Ciencia y Tecnología (UNSAM), Buenos Aires, Argentina
[bb]Instituto Argentino de Radioastronomía (CONICET, CIC), Buenos Aires, Argentina
[cc]GEMA (Universidad Nacional de La Plata), Buenos Aires, Argentina
[dd]California Institute of Technology, Pasadena, CA, USA
[ee]Institute of Technology Carlow, Carlow, Ireland
[ff]University of Science and Technology of Hanoi (USTH), Vietnam Academy of Science and Technology (VAST), Hanoi, VietNam

ABSTRACT

QUBIC (the Q&U Bolometric Interferometer for Cosmology) is a ground-based experiment which seeks to improve the current constraints on the amplitude of primordial gravitational waves. It exploits the unique technique, among Cosmic Microwave Background experiments, of bolometric interferometry, combining together the sensitivity of bolometric detectors with the control of systematic effects typical of interferometers. QUBIC will perform sky observations in polarization, in two frequency bands centered at 150 and 220 GHz, with two kilopixel focal plane arrays of NbSi Transition-Edge Sensors (TES) cooled down to 350 mK. A subset of the QUBIC instrument, the so called QUBIC Technological Demonstrator (TD), with a reduced number of detectors with respect to the full instrument, will be deployed and commissioned before the end of 2018.

The voltage-biased TES are read out with Time Domain Multiplexing and an unprecedented multiplexing (MUX) factor equal to 128. This MUX factor is reached with two-stage multiplexing: a traditional one exploiting Superconducting QUantum Interference Devices (SQUIDs) at 1 K and a novel SiGe Application-Specific Integrated Circuit (ASIC) at 60 K. The former provides a MUX factor of 32, while the latter provides a further 4. Each TES array is composed of 256 detectors and read out with four modules of 32 SQUIDs and two ASICs. A custom software synchronizes and manages the readout and detector operation, while the TES are sampled at 780 Hz (100kHz/128 MUX rate).

In this work we present the experimental characterization of the QUBIC TES arrays and their multiplexing readout chain, including time constant, critical temperature, and noise properties.

Keywords: Bolometric Interferometry, CMB instrumentation, Cosmic Microwave Background, SiGe Application-Specific Integrated Circuit, Superconducting QUantum Interference Device, the QUBIC experiment, Time-Domain Multiplexing, Transition-Edge Sensor

1. INTRODUCTION

The measurement of the tensorial component of the polarization of the Cosmic Microwave Background (CMB), the so called *B-modes*, is among the current targets of the Precision Cosmology. Its detection would provide valuable information about the primordial universe, inflation theory as well as quantum gravity. So far CMB experiments have only been able to place constraints on the amplitude of the inflationary parameter r. Currently observing CMB experiments (e.g. AdvACT,[1] POLARBEAR-2/Simons Arrays,[2,3] CLASS,[4] SPT-3G,[5] BICEP3[6]) and under design (BICEP Array[7] and Simons Observatory[8]) promise to improve even more the current upper limits on the amplitude of r. All of these experiments share the same working strategy: they are imagers. In such

Send correspondence to Maria Salatino. E-mail: maria.jokeating@gmail.com.

instrumental configuration, on the focal plane it is formed the sky image. The detectors on the focal plane collect all the parallel rays of light coming from a given selected frequency band; this reduces the photon noise. Imagers, therefore, are able to perform high sensitive observations of the sky thanks to background-limited broadband detectors. In interferometers what is formed on the focal plane are the Fourier modes of the sky radiation produced by an array of spatially correlated antennas. Generally, such instrumental configurations suffer low sensitivity and the impossibility of exploiting background-limited broadband detectors. The interferometers necessity of amplifying and down converting the signal increases the noise, while the presence of a correlator adds complexity in the instrument design. The great advantage of interferometric instruments resides in their capability of controlling systematic effects. Measurements of the scalar component of the CMB polarization, the E-modes, have been performed in the past with such instrumental configuration (CBI,[9] DASI[10]).

In this context, QUBIC currently presents a unique working strategy, combining together the sensitivity of bolometric detectors together with the control of systematic effects typical of interferometers. The optical combiner produces on the focal plane an image called *synthesized image*, resulting by specific Fourier modes selected by the receiving horns array. In this sense a bolometric interferometer can be considered a synthesized imager: the image on the focal plane is the synthesized beam formed by the array of receiving horns.

In QUBIC the sky signal is modulated by a cryogenic stepped Half-Wave Plate (HWP) followed by a fixed polarizer. An array of 400 back to back horns, a primary and secondary mirrors act as a Fizeau interferometer. A dichroic filter, tilted 45° with respect to the normal, splits the incoming signal in one transmitted and in one reflected focal plane working at a frequency bands centered at 150 and 220 GHz, respectively. Each focal plane is populated by 1,024 Transition-Edge Sensors (TESes) cooled down to 350 mK by a custom ^{3}He-^{4}He adsorption fridge.[11]

For a general overview of the experiment and bolometric interferometry see Battistelli et *al.*[12] and references therein. For the instrument design and its thermal architecture see the QUBIC Technical Report[13] and May et *al.*,[11] respectively. Updates on the current status of the experiment can be found in Mennella et *al.*[14] and in O'Sullivan et *al.*[15] Simulations of the optical combiner and the back to back horns array are described in O'Sullivan et *al.*[16]

In this paper we focus on the experimental characterization of a QUBIC detector array which consists of 256 TESes. The paper is organized as follows: in Sec. 2 we review the readout chain from the bolometric detectors to the warm readout electronics. Sec. 3 presents the experimental characterization of the QUBIC TES array P73. We conclude discussing our results and presenting future work in Sec. 4.

2. THE QUBIC READOUT CHAIN

A QUBIC detector array consists of 256 NbSi TESes with Pd absorbing grids fabricated on a 3 inch 500 μm thick Silicon on Insulator (SOI) wafer.[17] NbSi TESes and Al wiring are evaporated on a 1 μm thick Si_3N_4 membrane which is deposited on the SOI by low-pressure chemical vapour deposition. A 1 μm thick SiO_2 layer controls the back deep etching (DRIE) process of the SOI wafer, necessary to release the membrane, assuring uniform etching.

On each SOI wafer eight reference pixels are uniformly deposited on the side, see e.g. Fig. 3. These references currently based on the same NbSi thermometer as the TES, but without membrane, will be replaced by normal resistors. The successive readout of this insensitive to radiation pixel is used to remove the 1/f readout noise by *correlated double sampling* techniques. These pixels will therefore be used for calibration purposes and for checks of possible systematic effects. Moreover, we might calibrate them and use as thermometers on the array.

The QUBIC TESes are fabricated with the following target parameters: critical temperatures $T_c \sim 600$ mK, Noise Equivalent Power (NEP) $\sim 10^{-17}$ W/$\sqrt{Hz}$, and saturation power $P_{sat} \sim$ tens pW.

The array is cooled down in a laboratory testbed exploiting an Oxford Triton Dilution Refrigerator (DR), capable of reaching mixing chambers temperatures as low as 20 mK. A custom Copper support holds the array while keeps it in thermal contact with the DR mixing chamber plate. Given the value of the T_c, a heater on the mixing chamber plate suitably heats up the array at hundreds mK. An ^{241}Am radioactive source is mounted on the Copper cover of the array for probing both TES time constants and sensitivity to high-energy particles (Sec. 3.5).

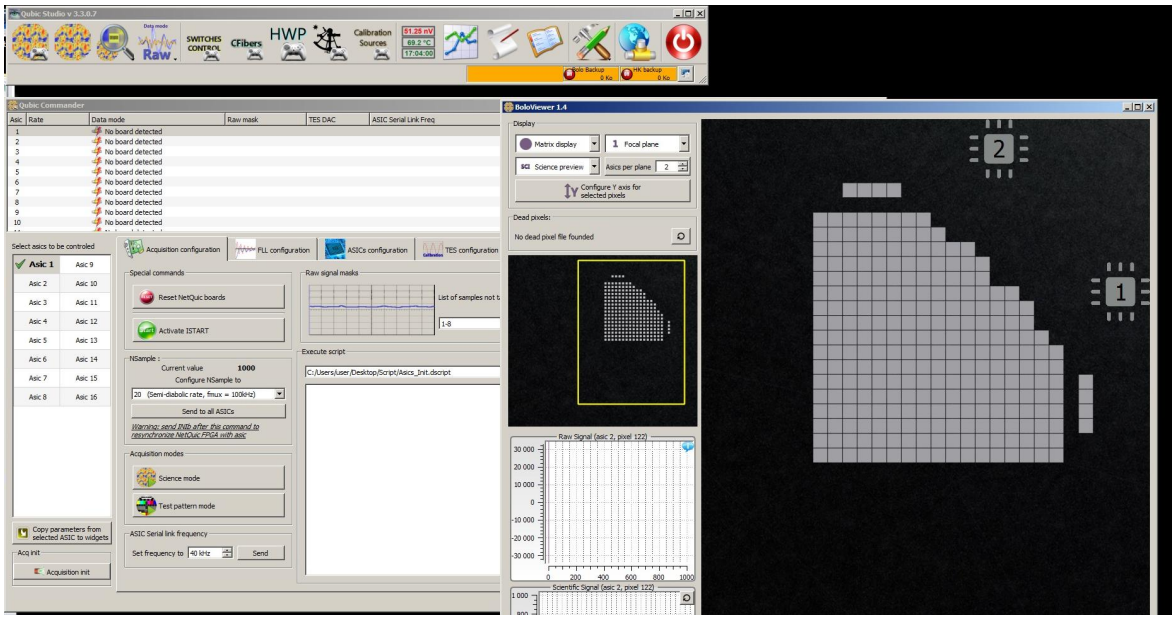

Figure 1: The QUBIC Studio software managing in real time TES operation.

The TESes are voltage-biased and read out with Time Domain Multiplexing (TDM) with the highest to date MUX factor, 128.[18] This readout architecture makes use of SQUID arrays mounted on the 2 K DR stage and of two ASICs on the 60 K DR stage. NbTi superconducting ribbon cables provide electrical contact between the 350 mK TES array, SQUID and ASIC stages. SQUIDs (custom based on SQ600 from STAR Cryoelectronics),[19] shunt resistors, electromagnetic interference filters, bias capacitors of the TDM are die bonded on Printed Circuit Boards (PCBs) which are mounted inside custom Al boxes at 2 K. Each board contain 32 SQUIDs, one per TES. Eight boards are necessary to read out one QUBIC TES array.

The TDM is organized in a matrix of 32 rows times 4 columns. A BiCMOS circuit sequentially biases each SQUID in a line through bias capacitors (Multiplexing - MUX - factor 32) while a SiGe ultra Low Noise Amplifier (LNA) read each column (MUX factor 4). The adjoint action of the addressing circuit and the LNA enables reaching the 128 MUX factor. Both the SQUID bias circuit and the LNA are hosted in an ASIC on the 60 K DR stage. One ASIC multiplexes 128 TESes, so two ASICs are required to read out one TES array. SQUIDs are kept on their operating point by a digital Flux Locked Loop (FLL).[18] A room temperature board, mounted outside the cryostat, synchronizes all the operations and provides the bias and the clocking of the ASIC.

A custom Windows software, QUBIC Studio (Fig. 1), developed in JavaScript, built upon the successful performance of the PILOT balloon-borne experiment,[20] manages the TDM, detector tuning operation and enables the real time look of the TES/SQUID signal.

3. EXPERIMENTAL CHARACTERIZATION

3.1 SQUID response

Each SQUID is die bonded on leaded PCB assembled in custom Al boxes.[18] Before the die bonding process, each SQUID is screened and normal resistance values are measured in a probe station at room temperature. After many tests we set to 200-300 Ω to be the acceptance resistance ranges for the SQUID itself, 13-15 $k\Omega$ for the input loop and 400-500 Ω for the feedback loop. These measurements essentially test the quality of the Nb access line deposition. At room temperatures, the access tracks dominate the resistance. Leakage resistances, especially between input loop and the SQUID washer, are also tested. Indeed, this is the main cause of malfunctioning of the readout chain. Any leakage resistances must be measured at a value larger than 20 MΩ at room temperature before the SQUID is die bonded with cryogenic epoxy. Typically, the yield of SQUIDs passing this room

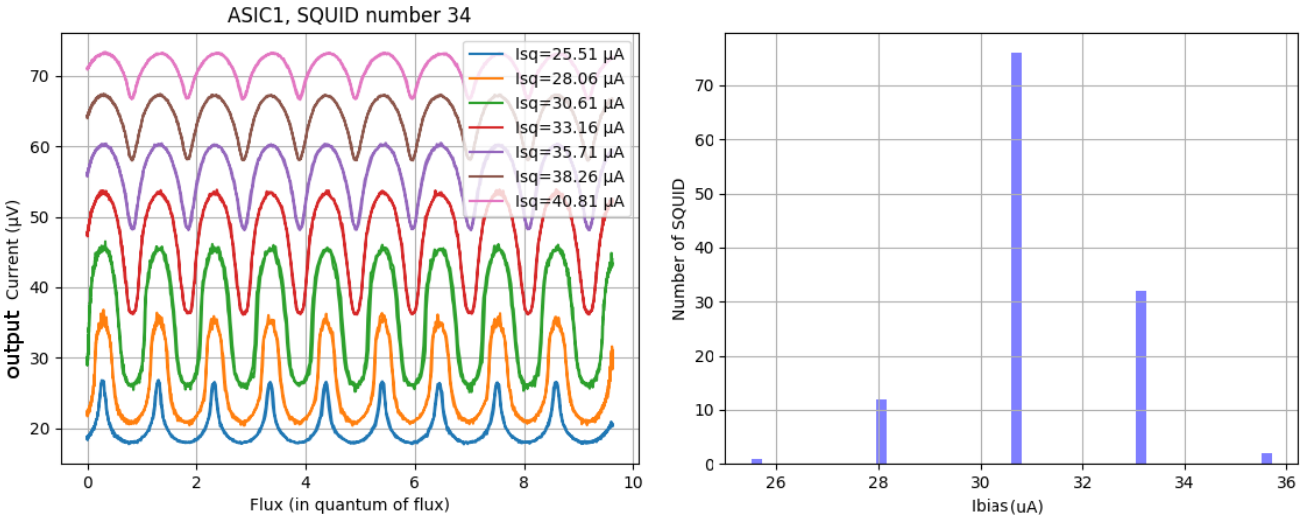

Figure 2: Left: typical current response of a QUBIC StarCRYO SQ600S SQUID (color figure online). Right: histogram of the SQUID response for each SQUID read out with ASIC1.

temperature tests is about 50 %. From testing the SQUID response versus input current (Fig. 2), we estimated a SQUID yield equal to 92.2 % for an optimal bias current of about 30-33 μA.
Because of the working principle of the ASIC, the input bias current values are discretized: to a given integer input value does not correspond an integer output bias current value. We have 15 possible integer values spanning the range $(0 \div 40.81)\mu$A. However, in practice, for biasing the SQUIDs we only use the last seven values which, being close to the critical current value (26 μA for our SQ600S SQUIDs), result in a nonzero SQUIDs response (Fig. 2, left).
The optimal bias current is selected as the value which maximizes the SQUIDs response for the greatest number of SQUIDs read out with the same ASIC, e.g.: the green curve corresponding to a bias current of 30.61 μA in Fig. 2, left. This value assures optimal behavior of about 62% of the SQUIDs against, for example, 24% for a 33.16 μA bias current value (Fig. 2, right). Therefore, we set 30.61 μA to be the optimal bias current. Fig. 2 refers to tests performed on ASIC1, however we expect similar performance and yield for SQUIDs on ASIC2. The selected optimal bias will be the same for both ASICs.

3.2 Parasitic and normal resistance

The existence of a parasitic resistance in series with the TES makes the detector resistance nonzero when it becomes superconducting and it affects the TES current value. Possible sources, difficult to estimate quantitatively, are wiring and wirebonds, for example. With the TESes superconducting at 300 mK we have estimated the value of the parasitic resistance injecting, in the TES biasing circuit, a sine wave 0.02 V wide with frequency 10 Hz. From the comparison of the input and output amplitudes we estimated the parasitic resistance. We found a very small difference in the median values of the two halves of the detector array (which are read out by two different ASICs, Sec. 2): 20 and 17 mΩ. These difference come from slightly lower resistance values for ASIC1 with respect to ASIC2 (Fig. 3, left). However, an overall spread of about 30 % (Fig. 3, right) and a final median value equal to 19 mΩ is not problematic.

Similarly, with the TESes on their normal branches, we have measured the normal resistance injecting, in the TES biasing circuit, a sine wave 0.1 V wide with frequency 10 Hz. In this case the measurement has to be performed with as high as possible MUX sampling rate (e.g. >20 kHz). These measurements have been performed at temperatures higher than $T_c \sim 600$ mK. A small disuniformity between the two halves of the array, present at 600 mK (one half is dominated by higher resistance values with respect to the other), disappears at temperatures higher than 600 mK. At 700 mK and with 20 kHz MUX sampling rate, we found median values equal to 1.08 and 1.06 Ω for ASIC1 and ASIC2, respectively (Fig. 4 left). Finally, the overall spatial distribution (Fig. 4 right) is in good agreement with what is expected from detectors fabrication.

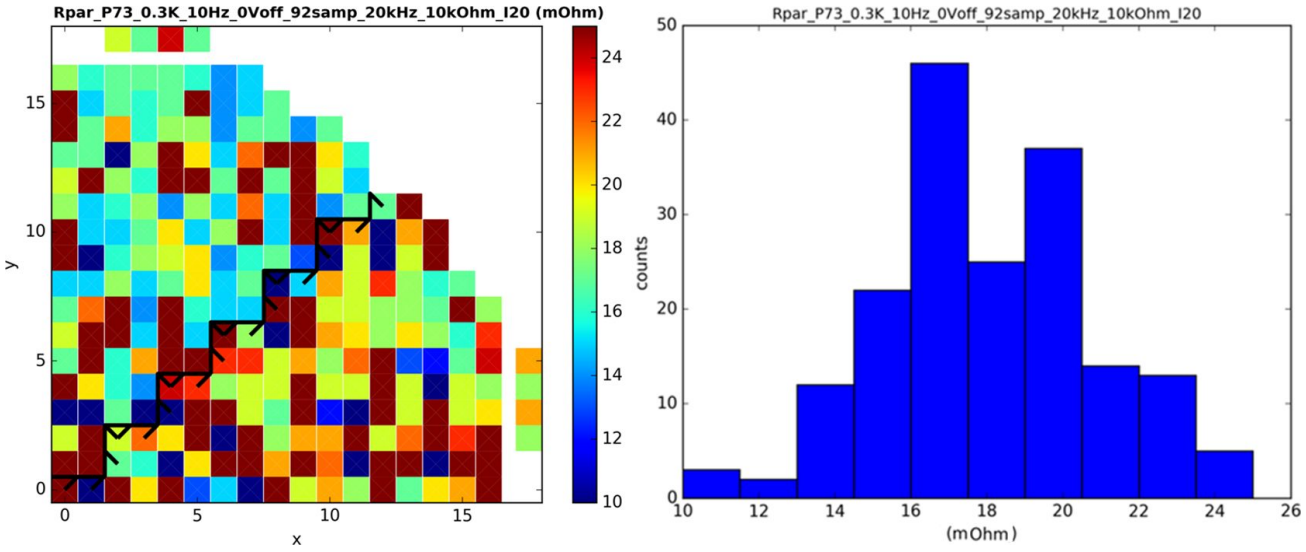

Figure 3: Parasitic resistance, $R_{\rm par}$, for array P73. Left: spatial distribution across the focal plane. Right: histogram (color figure online).

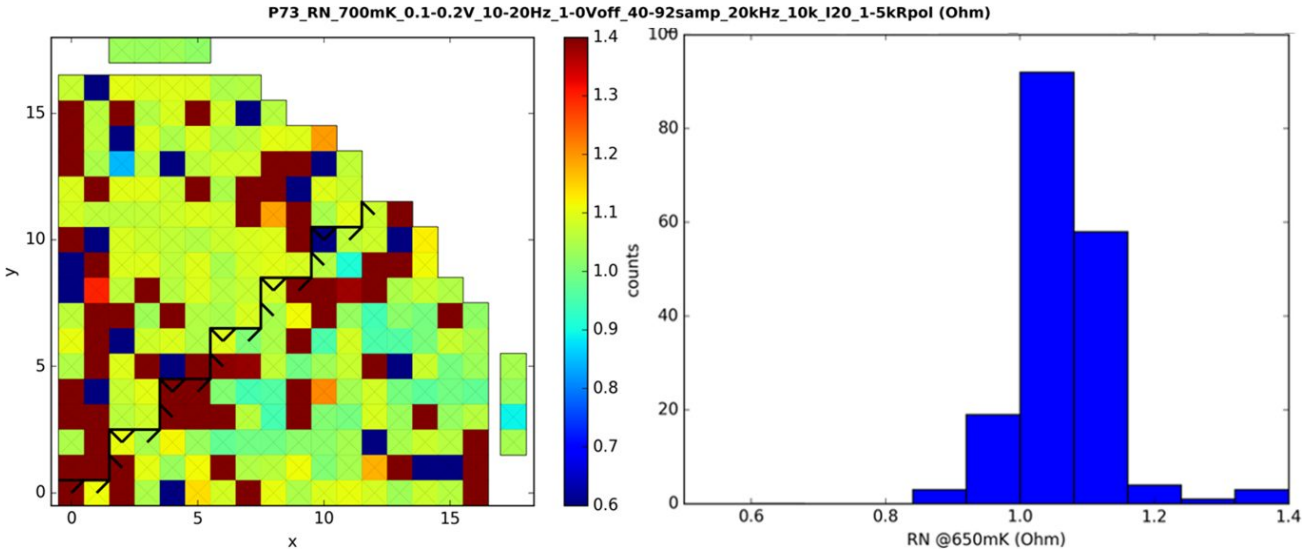

Figure 4: Normal resistance, R_N, at 700 mK for array P73. Left: spatial distribution across the focal plane. Right: histogram (color figure online).

The values of the parasitic and normal resistances will be used to improve the current-voltage (IV) calibration in the future detector tests.

3.3 TES biasing

The TES array is biased by a sine wave bias (Fig. 5), generated by the warm electronics, spanning the range $(3-9)$V. A biasing circuit ($R_{shunt} = 10m\Omega$, $R_{bias} = 10k\Omega$) reduces the input bias to the necessary μV range. The TES biasing with a sine wave bias produces a IV timeline with a series of primary (normal branch) and secondary (superconducting regime) maxima: a standard IV curve (from superconducting to normal regime) is, therefore, followed by a reversed one (from normal to superconducting regime), Fig. 5. By knowing the period of the bias signal sine wave (about 100 s) and by measuring the absolute maximum value in the IV timeline, one standard IV curve is then extracted.

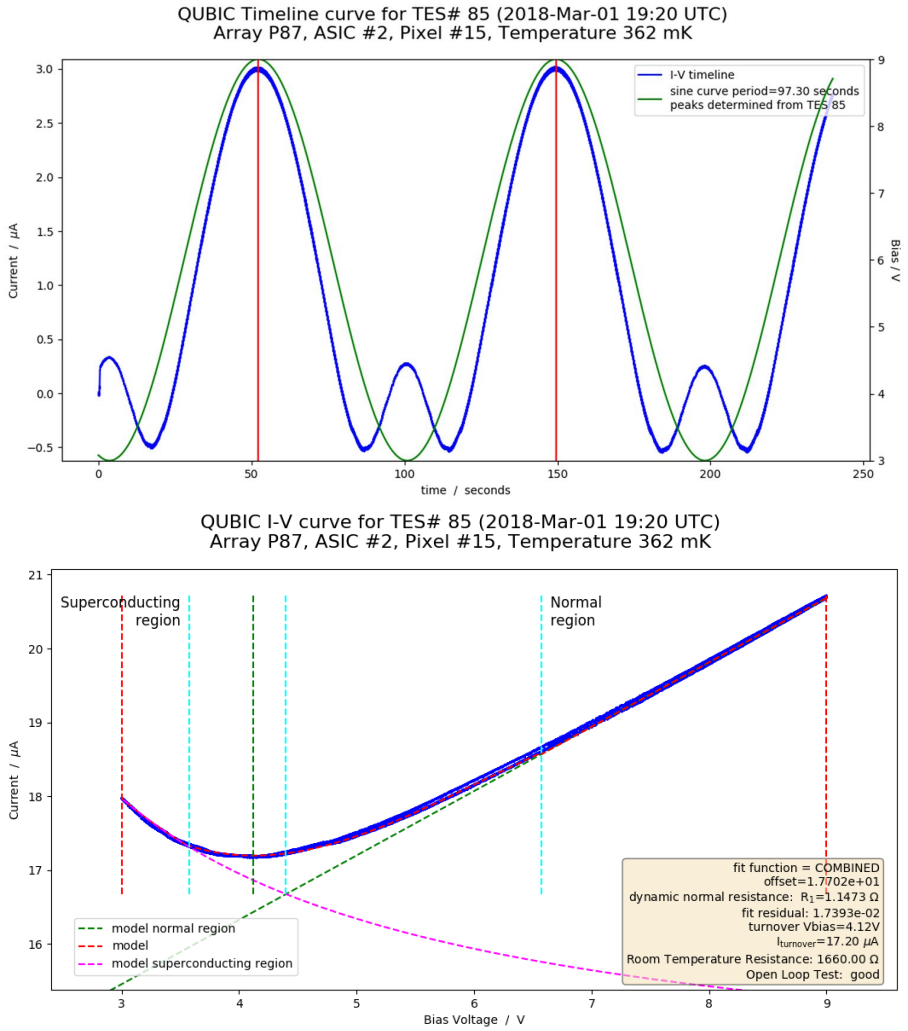

Figure 5: Top: A typical QUBIC bias signal sine wave (green line, right axis) with the corresponding TES response (blue line, left axis). Bottom: The reconstructed IV curve (blue line) with a fitted curve (magenta line in the superconducting region, green line in the normal region, and red line for the combined model (color figure online).

The TES voltage V_{TES} is estimated by the bias circuit. The IV calibration, i.e. the estimate of the DC offset for the SQUID feedback current, is performed fitting the normal branch with a linear fit and imposing $I_{TES} = 0$ for voltage bias $V_{bias} = 0$.[21]

3.4 TES parameters estimate

The bias power P_{bias} of a TES is traditionally related to the T_c by the empirical formula:[22]

$$P_{bias} = K(T_c^n - T_{bath}^n), \tag{1}$$

where T_{bath} is the bath temperature, K a constant, and n the index of the power law. The n value is strictly related to the signal carriers and generally has a value around 3.3. The TES thermal conductance is estimated from eq. (1) as:

$$G = \frac{dP_{bias}}{dT_c} = KnT_c^{n-1}. \tag{2}$$

The TES parameters (T_c, n, K) are estimated fitting eq. (1) upon a sweep in temperature of the TES array. Given the target T_c (Sec. 2), the sweep spans the temperature range $\sim (200 - 650)$ mK. To enable a reliable parameters estimate, the sweep in temperature is performed in steps of 30 or 50 mK. Given the low thermal conductivity of the SOI array substrate (Sec. 2), for each target temperature step we wait 20 min to be sure of the array thermalization. This conservative approach is also required by the absence of a thermometer on the array holder (the TES temperature is estimated from the Oxford $Ru0_2$ mixing chamber plate thermometer). TES parameters are estimated with a Minimum χ^2 method which provides the initial guess for a Monte Carlo Markov Chain (MCMC) algorithm (based on the Metropolis-Hasting MCMC algorithm[23,24]). Both algorithms have been suitably developed for the data analysis of the AdvACT detector arrays.[25]

An example of TES parameters estimated with the MCMC algorithm is reported in Fig. 6. The top right plot shows the measured $P_{bias}(T_{bath})$ values (black crosses) and the estimated fit from the MCMC (red line). The TES position on the QUBIC focal plane is shown in the right center plot. The likelihoods of the parameters is shown along the diagonal, while the bottom left plots show the contour plots, and so the correlation/degeneracy among the parameters. For all the detectors we estimated the TES parameters with the χ^2 minimizing algorithm followed by the MCMC algorithm. An example of the parameters distribution versus the position on the focal plane is reported in Fig. 7 for half of the array. The white squares denote detectors belonging to the deadlists.

3.5 Tests with ^{241}Am source

Performance of the HFI instrument on board of the Planck satellite were close to be limited by interactions between the bolometric detectors and the Cosmic Rays (CRs)[26] (see Fig. 4 in Catalano et *al.*[27]), especially high-energy alpha particles. This drove the necessity of testing detectors sensitivity towards CRs. With the target of testing QUBIC TESes sensitivity for possible future space applications, we have mounted, on the detectors holder, an ^{241}Am source extracted from common smoke detectors. This source is particularly suitable for our tests as its main decay products are alpha particles with 5.5 MeV energy. However, the time scales of the radioactive decay, fractions of seconds, allows to also use the source to measure the detectors time constant and to test the maximum sampling frequency our TDM readout can afford. Moreover, by fitting the TES response to the high-energy particle we have also estimated the energy of the alpha particles. The TES time constant also depends on the I parameter of the PID FLL.[28] We have estimated two time constants, the electric readout system time constant (τ_0), which is the rising time of a glitch, in the range and the thermal time constant (τ_1), which represents decay time of a glitch. Typical values for τ_0 and τ_1 are (10-20) ms and (30-60) ms, respectively. Moreover, we estimated the energy of the alpha particles in the range (2-5) MeV (Fig. 8), in agreement with theoretical predictions. Our results demonstrate the capability of our readout electronics in performing tests of sensitivity towards CRs.

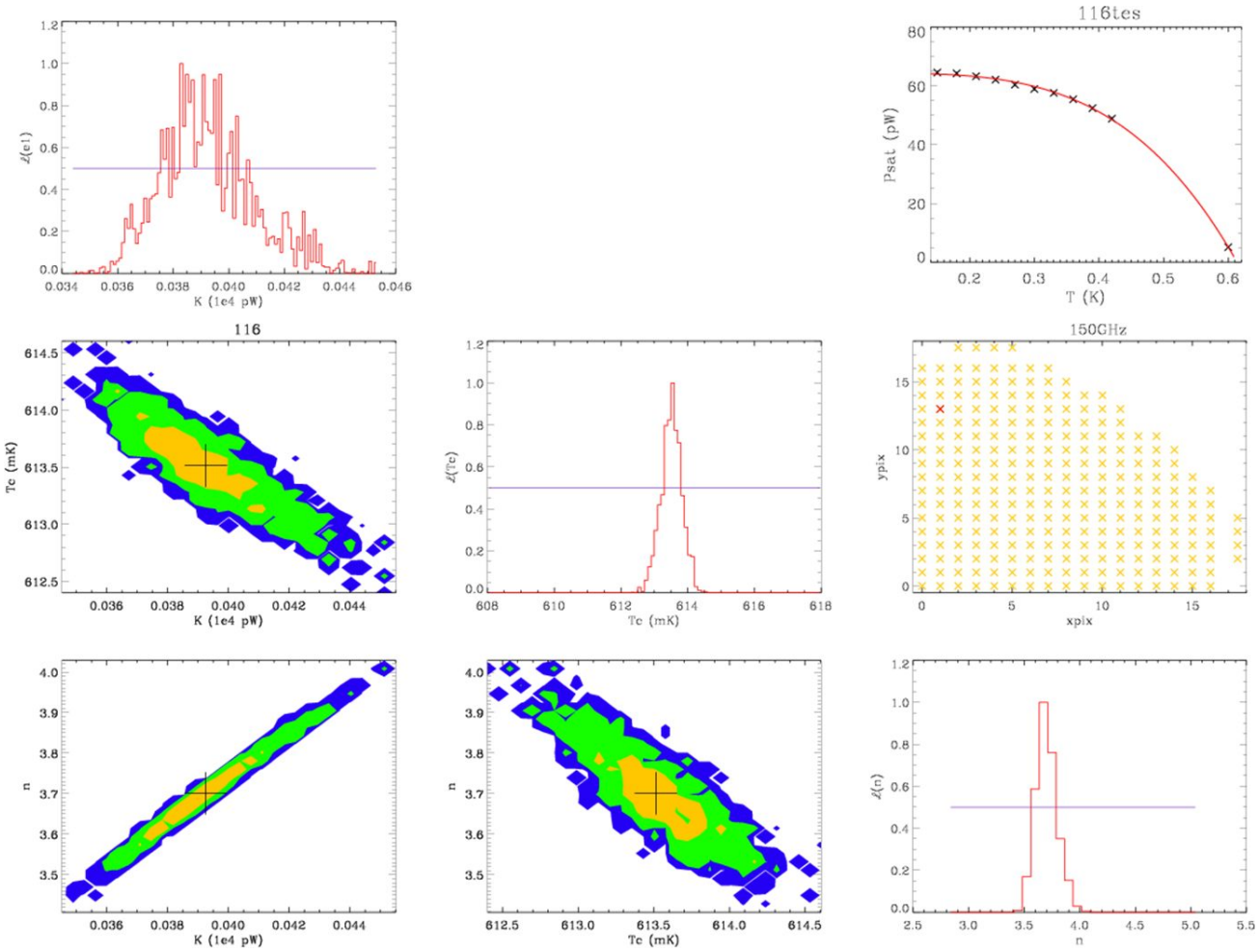

Figure 6: Parameters of a QUBIC TES estimated with a suitable MCMC algorithm developed for AdvACT[25] (color figure online). From top right to bottom left: experimental data and estimated theoretical fit, QUBIC detector array, TES parameters likelihoods and contour plots of the TES parameters.

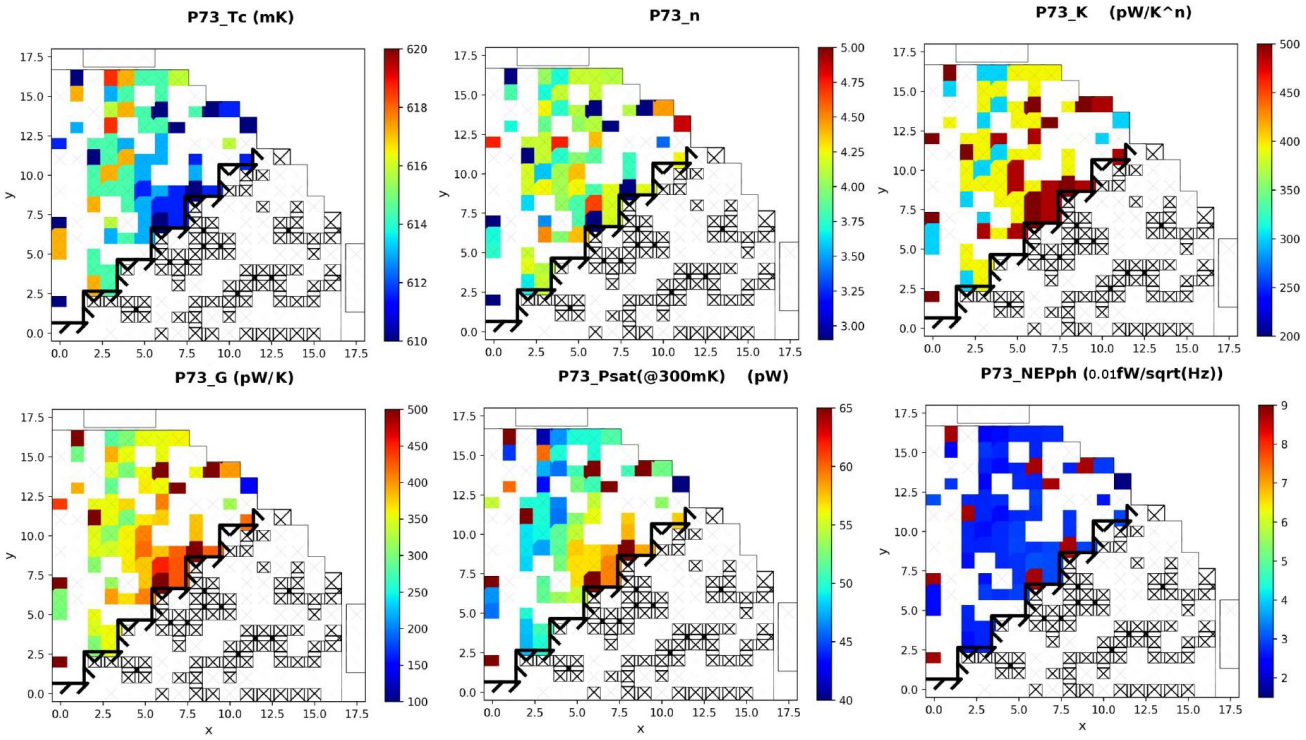

Figure 7: Spatial distribution of the QUBIC TESes parameters. From top left to bottom right: T_c, K, n, G, P_{sat}, phononic NEP (color figure online). The thick black line denotes the detector array sector read out with the same ASIC (Sec. 2). The four isolated pixels on top left and bottom right of the detectors array are the reference pixels.

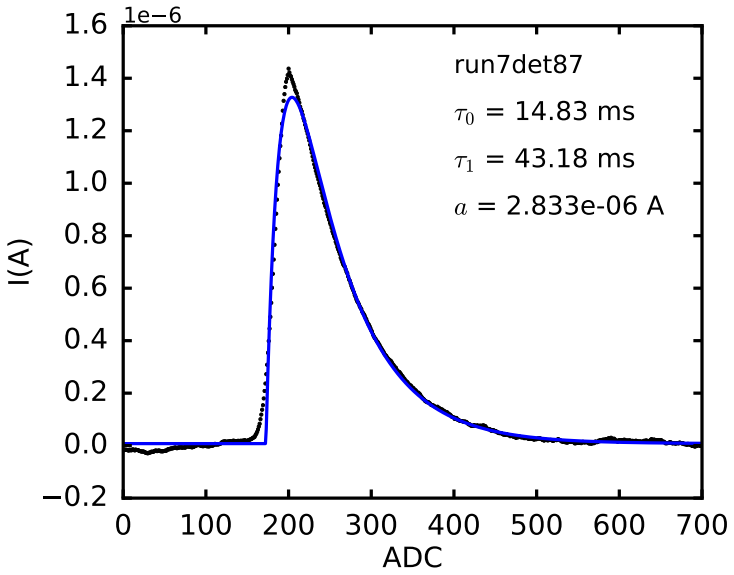

Figure 8: QUBIC TES response towards alpha particles emitted by an ^{241}Am source. The black dot line is the experimental data number 7 and detector number 87. The data is stacked of all glitches in a timeline of $\sim$ 10 minutes. The blue curve represents the exponential fitted functions (color figure online).

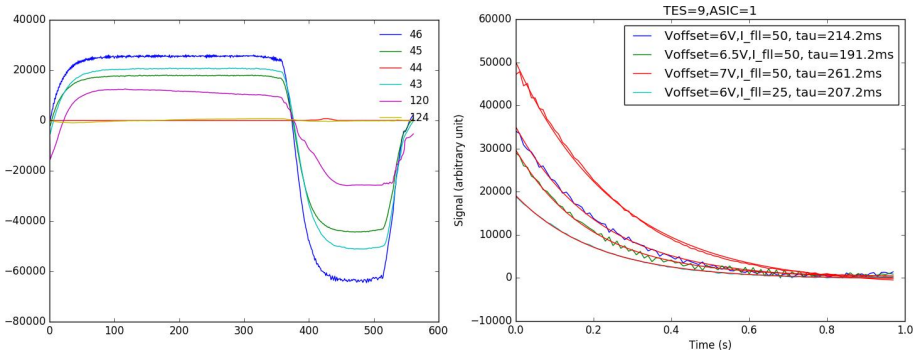

Figure 9: Left: Stacked pulses measured for different TESes, array P73, once they are illuminated by a Carbon fiber. Right: Detector response to the Carbon fiber signal versus the I PID FLL parameter (color figure online).

3.6 Tests with Carbon fiber

A Carbon fiber,[29] similar to the ones used to calibrate the Archeops and Planck-HFI instruments, has been installed in front of the P73 TES array to provide a first optical test of detectors. The fiber is heated by Joule effect through a square pulsed current generator. The typical stacked signal is shown on Fig. 9 (left) for several TESes. We have estimated a detectors yield of about 72% over the full array. The detectors response for different values of the I FLL PID parameter is shown in Fig. 9 right. Typically, the Carbon fiber used for those tests has a time constant of about 200 ms. By fitting the TES output signal for different I values of the FLL PID, we have checked the uniformity of the detectors optical response. Two Carbon fibers will be installed in the QUBIC cryostat, with a smaller time response (of the order of a few ms) to further cross-check the alignment between the horn and switches arrays[12,13] (on the edges of which the fibers will be installed) and the focal plane. They will also allow to cross-check and to monitor the relative calibration of the TESes.

4. CONCLUSION AND FUTURE WORK

In this paper we have demonstrated the capability of a TDM architecture with MUX factor 128 in reading out TESes arrays. Suitable softwares for the QUBIC detector arrays characterization have been developed. The softwares will be used both for laboratory characterization as well as commissioning on the field. At the time of writing the QUBIC cryostat is being integrated at the AstroParticle and Cosmology (APC) laboratory in Paris. Therefore, the experimental characterization of the detector arrays integrated in the TD is going to be performed in the next months, prior to the deployment on the QUBIC operation site.

ACKNOWLEDGMENTS

The APC team acknowledges the financial support of the UnivEarthS Labex program at Sorbonne Paris Cité (ANR-10-LABX-0023 and ANR-11-IDEX-0005-02).

REFERENCES

[1] S.W. Henderson et *al.*, "Advanced ACTPol Cryogenic Detector Arrays and Readout," *Journal Low Temp. Phys.* **184**(3-4), p. 772, 2016. astro-ph/1510.02809.

[2] A. Suzuki et *al.*, "The POLARBEAR-2 and the Simons Array Experiments," *JLTP* **184**(3-4), pp. 805–810, 2016. astro-ph/1512.07299.

[3] Y. Inoue et *al.*, "POLARBEAR-2: an instrument for CMB polarization measurements," *Proc. SPIE* **9914**, p. 99141I, 2016. astro-ph/1608.03025.

[4] T. Essinger-Hileman et *al.*, "CLASS: the cosmology large angular scale surveyor," *Proc. SPIE* **9153**, p. 91531I, 2014. astro-ph/1408.4788.

[5] B.A. Benson et *al.*, "SPT-3G: a next-generation cosmic microwave background polarization experiment on the South Pole telescope," *Proc. SPIE* **9153**, p. 91531P, 2016. astro-ph/1407.2973.

[6] H. Hui et *al.*, "BICEP3 focal plane design and detector performance," *Proc. SPIE* **9914**, p. 99140T, 2016. astro-ph/1607.06861.
[7] J.A Grayson et *al.*, "BICEP3 performance overview and planned Keck Array upgrade," *Proc. SPIE* **9914**, p. 99140S, 2016. astro-ph/1607.04668.
[8] N. Galitzki et *al.*, "The Simons Observatory cryogenic cameras," *Submitted to SPIE* , 2018.
[9] S. Padin et *al.*, "The Cosmic Background Imager," *PASP* **114**, pp. 83–97, 2002.
[10] N.W. Halverson et *al.*, "DASI: Degree Angular Scale Interferometer for imaging anisotropy in the cosmic microwave background," *Proc. SPIE* **3357**, pp. 416–423, 1998.
[11] May A. et *al.*, "Thermal architecture for the QUBIC cryogenic receiver," *Submitted to SPIE* , 2018.
[12] E.S. Battistelli et *al.*, "QUBIC: The QU bolometric interferometer for cosmology," *Astroparticle Physics* **34**, pp. 705–716, 2011. astro-ph/1010.0645.
[13] The QUBIC Collaboration, "QUBIC Technical Design Report," 2016. astro-ph/1609.04372.
[14] A. Mennella et *al.*, "QUBIC - The Q&U Bolometric Interferometer for Cosmology. A novel way to look at the polarized Cosmic Microwave Background.," *EPS Conference on High Energy Physics* , 2018. astro-ph/1801.03730.
[15] O'Sullivan et *al.*, "QUBIC: The Q&U Bolometric Interferometer for Cosmology," *Submitted to SPIE* , 2018.
[16] O'Sullivan et *al.*, "Simulations and performance of the QUBIC optical beam combiner," *Submitted to SPIE* , 2018.
[17] C. Perbost et *al.*, "A 256-TES Array for the Detection of CMB B-Mode Polarisation," *Journal of Low Temp Physics* **184**, pp. 793–798, 2016.
[18] D. Prêle et *al.*, "A 128 Multiplexing Factor Time-Domain SQUID Multiplexer," *Journal of Low Temp Physics* **184**, pp. 363–368, 2016.
[19] STAR Cryoelectronics website: https://starcryo.com.
[20] J.-P. Bernard et *al.*, "PILOT: a balloon-borne experiment to measure the polarized FIR emission of dust grains in the interstellar medium," *Experimental Astronomy* **42**, pp. 199–227, 2016.
[21] E. Grace, "Detector characterization, optimization, and operation for ACTPol," *PhD Thesis. Princeton University* , 2016.
[22] K. Irwin and G. Hilton, *Transition-Edge Sensors*, vol. 99, Springer, 2005.
[23] C. Andrieu, N. De Freitas, A. Doucet et *al.*, "An Introduction to MCMC for Machine Learning," *Kluwer Academic Publishers* **50**, pp. 5–43, 2003.
[24] D. J. C. MacKay, *Information Theory, Inference, and Learning Algorithms.*, Cambridge Univ. Press., 2003.
[25] M. Salatino et *al.*, "Investigations on kilopixel focal planes directed toward improving next-generation instruments," *In preparation* , 2018.
[26] Planck Collaboration, "Planck 2013 results. X. HFI energetic particle effects: characterization, removal, and simulation," *A&A* **571**, p. A10, 2014. astro-ph/1303.5071.
[27] A. Catalano et *al.*, "Characterization and Physical Explanation of Energetic Particles on Planck HFI Instrument," *Journal of Low Temp. Phys.* **176**, pp. 773–786, 2014. astro-ph/1403.5639.
[28] D. Hoang *PhD Thesis. Paris Diderot University, in prep.* , 2018.
[29] S. Henrot-Versillé et *al.*, "Pulsed carbon fiber illuminators for FIR instrument characterization," *Infrared Physics & Technology* **52**, pp. 159–165, 2009.